MATERIALS SCIENCE

Enabling full-scale grain boundary mitigation in polycrystalline perovskite solids

Lichen Zhao[1,2]†, Pengyi Tang[3,4]†, Deying Luo[1], M. Ibrahim Dar[5]*, Felix T. Eickemeyer[2], Neha Arora[5]§, Qin Hu[6,7,8]*, Jingshan Luo[2,9], Yuhang Liu[2]*, Shaik Mohammed Zakeeruddin[2], Anders Hagfeldt[10]‡, Jordi Arbiol[3,11], Wei Huang[12,13], Qihuang Gong[1,14], Thomas P. Russell[6,7], Richard H. Friend[5], Michael Grätzel[2]*, Rui Zhu[1,14]*

Copyright © 2022 The Authors, some rights reserved; exclusive licensee American Association for the Advancement of Science. No claim to original U.S. Government Works. Distributed under a Creative Commons Attribution NonCommercial License 4.0 (CC BY-NC).

There exists a considerable density of interaggregate grain boundaries (GBs) and intra-aggregate GBs in polycrystalline perovskites. Mitigation of intra-aggregate GBs is equally notable to that of interaggregate GBs as intra-aggregate GBs can also cause detrimental effects on the photovoltaic performances of perovskite solar cells (PSCs). Here, we demonstrate full-scale GB mitigation ranging from nanoscale intra-aggregate to submicron-scale interaggregate GBs, by modulating the crystallization kinetics using a judiciously designed brominated arylamine trimer. The optimized GB-mitigated perovskite films exhibit reduced nonradiative recombination, and their corresponding mesostructured PSCs show substantially enhanced device efficiency and long-term stability under illumination, humidity, or heat stress. The versatility of our strategy is also verified upon applying it to different categories of PSCs. Our discovery not only specifies a rarely addressed perspective concerning fundamental studies of perovskites at nanoscale but also opens a route to obtain high-quality solution-processed polycrystalline perovskites for high-performance optoelectronic devices.

INTRODUCTION

Polycrystalline halide perovskite solids have emerged as excellent semiconductor materials for photovoltaics (*1*, *2*), light-emitting diodes (*3*, *4*), lasers (*5*), and photodetectors (*6*) because of their ease of fabrication and outstanding optoelectronic properties (*7*–*9*). The polycrystalline nature of the perovskites arising from rapid nucleation and crystallization from solution at relatively low temperatures usually causes a considerable density of grain boundaries (GBs). In a typical polycrystalline film, a grain is a single-crystalline entity, and a GB is the interface between two individual homophase crystal grains of the same material that are generally oriented in different crystallographic directions according to the classic material science textbooks (*10*, *11*). The aggregation of grains is inevitable in this polycrystalline film (*12*). The grain aggregates, in turn, form larger agglomerates (domains) leading to domain boundaries, often and inadequately referred to as "GBs" in the research field of metal halide perovskites. As shown in Fig. 1A, these resultant boundaries can be categorized as interaggregate GBs (pointed by green arrows) and intra-aggregate GBs (indicated by orange arrows), respectively.

The interaggregate GBs have been frequently and extensively examined in metal halide perovskite research as they can be readily observed by optical microscopy, scanning electron microscopy (SEM), or scanning probe microscopy (*13*–*15*). By contrast, the number of crystallographic studies on the genuine GBs at nanoscale and the structural heterogeneity inside grain aggregates by transmission electron microscopy (TEM) is limited to date. Previous studies mainly concerned the interaggregate GBs as they may adversely affect the charge carrier transport, facilitate ion migration, and even produce some deep sub-band energy levels within the bandgap (*16*, *17*), leading to major nonradiative losses that limit the photovoltaic performance (*13*, *18*, *19*). In addition, some imperfect structures occurring at interaggregate GBs may influence the device stability associated with the presence of mobile charges or ions, oxygen, moisture, heat, and light (*20*–*24*). In this regard, many approaches, such as surface passivation and functionalization (*25*, *26*), have been widely studied to suppress these undesirable defects at interaggregate GBs.

Recently, the existence of grain aggregates and intra-aggregate GBs has been confirmed by electron backscatter diffraction and TEM (*27*–*31*). Li *et al.* (*29*) and Cai *et al.* (*30*) start to correlate the performances of perovskite solar cells (PSCs) with the density and structure of intra-aggregate GBs in polycrystalline perovskite films. These intra-aggregate heterogeneities have been validated to evoke detrimental effects on the performances of PSCs including power conversion efficiency (PCE), open-circuit voltage (V_{OC}), current density–voltage (J–V) hysteresis, and stability of PSCs, implying that the mitigation

[1]State Key Laboratory for Artificial Microstructure and Mesoscopic Physics, School of Physics, Frontiers Science Center for Nano-optoelectronics & Collaborative Innovation Center of Quantum Matter, Peking University, Beijing 100871, China. [2]Laboratory of Photonics and Interfaces, Institute of Chemical Sciences and Engineering, École Polytechnique Fédérale de Lausanne, Station 6, CH-1015 Lausanne, Switzerland. [3]Catalan Institute of Nanoscience and Nanotechnology (ICN2), CSIC and BIST, Campus UAB, Bellaterra, Barcelona 08193, Catalonia, Spain. [4]State Key Laboratory of Information Functional Materials, 2020 X-Lab, ShangHai Institute of Microsystem and Information Technology, Chinese Academy of Sciences, Shanghai 200050, China. [5]Cavendish Laboratory, Department of Physics, University of Cambridge, JJ Thomson Avenue, Cambridge CB3 0HE, UK. [6]Polymer Science and Engineering Department, University of Massachusetts, Amherst, MA 01003, USA. [7]Materials Sciences Division, Lawrence Berkeley National Laboratory, Berkeley, CA 94720, USA. [8]School of Microelectronics, University of Science and Technology of China, Hefei 230026, China. [9]Institute of Photoelectronic Thin Film Devices and Technology, Solar Energy Research Center, Nankai University, Tianjin 300350, China. [10]Laboratory of Photomolecular Science, Institute of Chemical Sciences and Engineering, École Polytechnique Fédérale de Lausanne, Station 6, CH-1015 Lausanne, Switzerland. [11]ICREA, Pg. Lluís Companys 23, Barcelona 08010, Catalonia, Spain. [12]Key Laboratory of Flexible Electronics & Institute of Advanced Materials, Jiangsu National Synergetic Innovation Center for Advanced Materials, Nanjing Tech University, Nanjing 211816, China. [13]Shaanxi Institute of Flexible Electronics, Northwestern Polytechnical University, Xi'an 710072, China. [14]Collaborative Innovation Center of Extreme Optics, Shanxi University, Taiyuan 030006, China.
*Corresponding author. Email: iamzhurui@pku.edu.cn (R.Z.); qinhu20@ustc.edu.cn (Q.H.); yuhang.liu@epfl.ch (Y.L.); id338@cam.ac.uk (M.I.D.); michael.graetzel@epfl.ch (M.G.)
†These authors contributed equally to this work.
‡Present address: Department of Chemistry-Ångström Laboratory, Uppsala University, Box 523, SE-751 20 Uppsala, Sweden.
§Present address: Department of Chemistry, University College London, 20 Gordon Street, London WC1H 0AJ, UK.

Downloaded from https://www.science.org at Universitat Autonoma de Barcelona on February 01, 2023

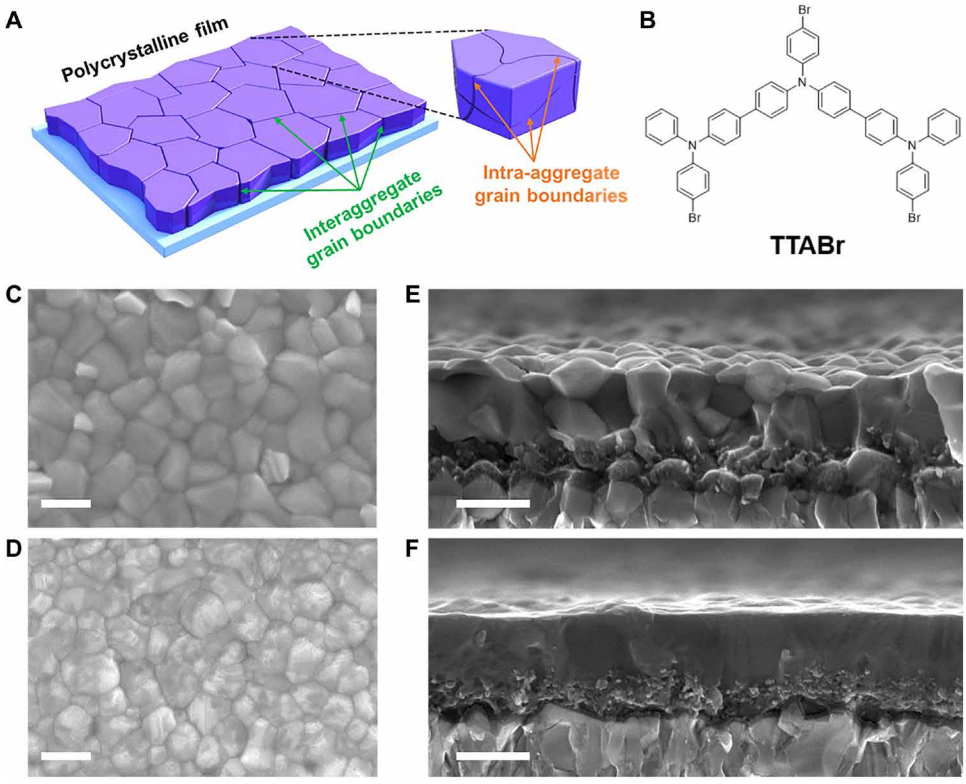

Fig. 1. Illustration of solid polycrystalline films and perovskite film morphologies. (**A**) Schematic diagram of a solid polycrystalline film with GBs, illustrating interaggregate GBs and intra-aggregate GBs. (**B**) Chemical structure of TTABr. (**C** and **D**) Top-view SEM images of the control (C) and GBMP (D) films. (**E** and **F**) Cross-sectional SEM images of the control (E) and GBMP (F) films. Scale bars, 400 nm (C to F).

of intra-aggregate GBs is of equal significance to that of interaggregate GBs. Full-scale mitigation from intra- to interaggregate GBs is thus urgently warranted to maximize the device performances toward theoretical limit. However, the deficient understanding of the fundamental origin of GBs renders it hard to develop effective full-scale GB mitigation strategies.

Here, we first systematically perform the crystallographic study on the grain aggregates and GBs, and we show full-scale GB mitigation from genuine GBs formed between small nanocrystals to interaggregate GBs in polycrystalline perovskite solids. We control precisely the crystal growth during the film formation process through the introduction of the brominated arylamine trimer N^4,$N^{4\prime}$-bis(4-bromophenyl)-N^4-(4′-((4-bromophenyl)(phenyl)amino)-[1,1′-biphenyl]-4-yl)-$N^{4\prime}$-phenyl-[1,1′-biphenyl]-4,4′-diamine (TTABr; Fig. 1B). A unique feature of TTABr is its solubility in both polar and nonpolar solvents used for dissolving in the perovskite precursors and as antisolvent, respectively. This enables it to act as a crystallization aid and to access GB sites, allowing it to mitigate defects. This results in the suppression of nonradiative carrier recombination, increasing substantially the V_{OC} of PSCs. By virtue of its more favorable redox potential, TTABr also enhances intergrain hole transfer, improving charge carrier collection and the fill factor (FF) of the devices. We analyze the detailed crystallographic information and link the underlying GB mitigation to the variation in microscopic structures, crystal size distributions, defect concentrations, charge carrier lifetimes, and photovoltaic performances. We demonstrate regular mesostructured perovskite photovoltaics based on GB-mitigated films with large enhancements in the device efficiency from 21.1 to 23.2% and long-term operational stability under illumination, humidity, or heat stress. The versatility of our strategy is also verified by applying it to different categories of PSCs. This discovery specifies a previously unaddressed perspective concerning the full-scale mitigation of GBs in perovskites from nanoscale to submicroscale, opening a route to obtain high-quality solution-processed polycrystalline perovskite films for high-performance optoelectronic devices.

RESULTS

Structure characterizations of perovskite films

Mixed-cation halide perovskites have shown their superiority in photovoltaic performance, delivering record-level certified PCEs over a brief period in the perovskite research community (*32*–*35*). Here, we focus on the mitigation of GBs for mixed-cation lead mixed-halide perovskite films with the composition of $FA_{0.851}MA_{0.149}PbI_{2.552}Br_{0.448}$ with 4.48 mole percent (mol %) excess PbI_2, where MA and FA denote methylammonium and formamidinium, respectively, via the intervention of the brominated arylamine trimer, TTABr. TTABr was fully characterized by mass spectrometry (MS) and nuclear magnetic resonance (NMR) spectroscopy. The differential scanning calorimetry (DSC) and thermogravimetry (TG) analyses (fig. S1) further reveal its good thermal stability. The GB-mitigated perovskite is abbreviated as "GBMP" below.

We first investigated the morphological variation of the control and GBMP films using SEM. Top-view SEM images in Fig. 1 (C and D)

Downloaded from https://www.science.org at Universitat Autonoma de Barcelona on February 01, 2023

show that the films with and without TTABr exhibit remarkably different surface morphologies. The control film is dominated by tightly packed angular blocks with sizes of ~200 to 400 nm. As mentioned above, these blocks observed with SEM are not single-crystalline grains but rather grain aggregates. We verified this by cross-sectional TEM analysis of the lamellae obtained from the devices with and without TTABr (fig. S2). The resulting interaggregate boundaries formed during crystal growth in the control film exhibit broken-line features, whereas, as shown in Fig. 1D, the angular nature of the GBMP film is substantially impaired as the grain aggregate outlines become rounded. The corresponding atomic force microscopy (AFM) and conductive AFM (c-AFM) images (fig. S3) of perovskite surfaces indicate larger current flow in the GBMP film than in the control and the GBs in GBMP film showing darker contrast. From the cross-sectional SEM images in Fig. 1 (E and F), we note that there are noticeable interaggregate boundaries across the control film, resembling the surface morphology. However, the GBMP film shows few obvious visible interaggregate boundaries across the entire cross section. We consider these differences to be related to the intervention of TTABr.

To access the crystalline phase evolution of the grain aggregates in the absence and presence of TTABr, we carried out the cross-sectional TEM measurements of the devices prepared with and without GBMP films. After systematically analyzing the high-resolution TEM (HRTEM) images and the corresponding temperature-colored fast Fourier transform (FFT) patterns as displayed in Fig. 2 and figs. S2 and S4, we confirm that both the control and GBMP films contain two different phases, including a tetragonal phase with space group 140 (*I*4/*MCM*) and a cubic phase with space group 221 (*PM*3*M*) (*36*, *37*), which is similar to the single-cation perovskites reported previously in the literature (*38*). Moreover, the HRTEM images and the corresponding temperature-colored FFT patterns in Fig. 2A (1 to 3) and figs. S2, S4A, and S5A demonstrate the polycrystalline nature for these observed regions of fixed size in the control film, whereas for the GBMP film (Fig. 2B, 1 to 3, and figs. S4B and S5B), the single-crystalline nature is realized for the observed regions of equivalent size.

It is noteworthy that the whole GBMP film containing TTABr is not a single crystal as some regions without a crystallographic texture are observed lying between different perovskite grains (Fig. 2C), whereas for the control film, we will obtain the overlapped imaging of all the stacked perovskite grains in the observation region from the vertical direction (i.e., parallel to the electron beam direction) in the HRTEM image. This hinders the atomic visualization of detailed structure for GBs in the control lamellae based on the two-dimensional (2D) TEM images. The amorphous structures localized at GBs are highlighted in white dotted lines in Fig. 2C and shown in fig. S5C. The prevalent single-crystalline perovskite nature observed in the HRTEM images obtained from the GBMP film confirms its larger grain sizes in comparison to the control film since the control film shows the polycrystalline nature in the commensurate field of view. In addition, by applying Scherrer equation to the most intense reflection in x-ray diffraction (XRD) pattern, i.e., (110) peak, we roughly estimated an average grain size of 72 nm for the GBMP sample, which is substantially larger than the grain size of 42 nm estimated for the control sample (fig. S6). The increased grain sizes are indicative of the reductions in the density of GBs and unwanted defects in the polycrystalline films.

To corroborate the reproducibility and reliability of TEM observations, we also probed crystallographic information via HRTEM images and FFT patterns in different regions of an identical sample

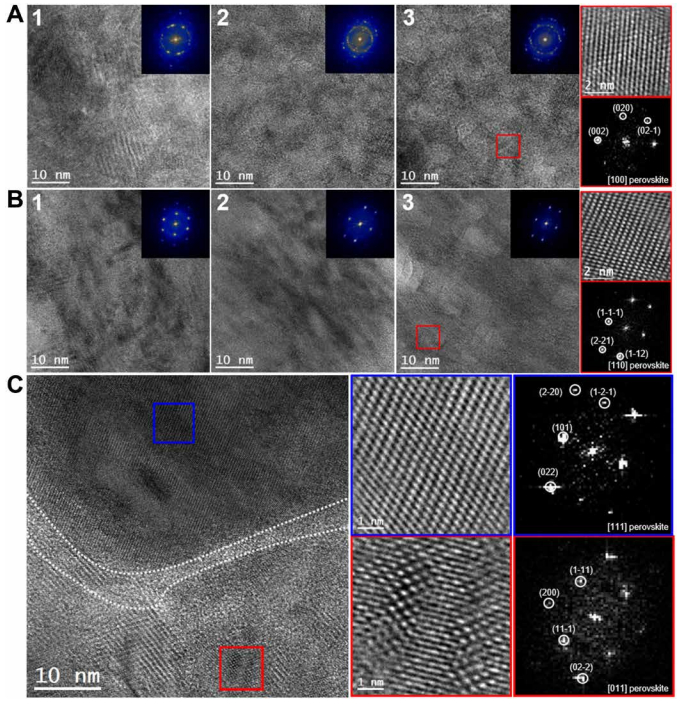

Fig. 2. Direct observations of perovskite grains, grain aggregates, and intra-aggregate GBs. (**A**) (1 to 3) Three representative HRTEM images and the corresponding temperature-colored FFT patterns from the control film. Right: The magnified HRTEM image of the red squared area selected in (A3) and the corresponding FFT pattern. It indicates that the crystal structure corresponds to a cubic perovskite phase with space group 221 (*PM*3*M*) visualized from [100] direction. (**B**) (1 to 3) Three representative HRTEM images and the corresponding temperature-colored FFT patterns from the GBMP film. Right: The magnified HRTEM image of the red squared area selected in (B3) and the corresponding FFT pattern. It indicates that the crystal structure corresponds to a cubic perovskite phase with space group 221 (*PM*3*M*) visualized from [110] direction. (**C**) Left: Representative HRTEM image of the region with intra-aggregate GBs of the GBMP film. Right top: The magnified HRTEM of the blue squared area and the corresponding FFT pattern. It indicates that the crystal structure corresponds to a cubic perovskite phase with space group 221 (*PM*3*M*) visualized from [111] direction. Right bottom: The magnified HRTEM of the red squared area and the corresponding FFT pattern. It indicates that the crystal structure corresponds to a cubic perovskite phase with space group 221 (*PM*3*M*) visualized from [011] direction.

and of different samples in various batches (fig. S5). All the HRTEM and FFT results show that the GBMP film indeed has larger perovskite grain sizes, delivering lower GB densities. By combining SEM and TEM results, we obtained a consistent result of mitigation in the density of intra-aggregate GBs. From HRTEM and FFT measurements, we also observe that there are isolated lead halide species [triclinic phase with space group 186 (*P*63*MC*)] with the sizes ranging from several nanometers to tens of nanometers distributed across the whole cross section of the control film (fig. S7). This is not unexpected since the films were processed from a nonstoichiometric perovskite precursor solution with excess lead halide. Our TEM results provide direct evidence that the lead halide species are embedded in the perovskite grain aggregates distributed in the whole film (fig. S8).

We further conducted annular dark-field scanning TEM (ADF-STEM) and electron energy-loss spectroscopy (EELS) measurements (*4*, *25*) to probe the spatial distribution of TTABr in the GBMP film.

Downloaded from https://www.science.org at Universitat Autonoma de Barcelona on February 01, 2023

As shown in the cross-sectional low-magnification STEM image of the GBMP film (Fig. 3A) and the control film (fig. S9A), there are some dark "gaps" with low *Z* contrast, indicating fewer perovskite species or lighter species. In the case of the control film, we do observe some interaggregate domain boundaries present outside the packed angular grain aggregates via SEM, suggesting that the dark gaps observed in the STEM for the control film arise from a lack of perovskite material at the interaggregate (domain) boundary sites. By contrast, the cross-sectional SEM image of the GBMP film exhibits fewer interaggregate boundaries, indicating that the dark zones observed by STEM of the GBMP films originate from TTABr embedded in the boundary regions. This is consistent with the HRTEM evidence for the presence of amorphous regions in the GBMP film.

From the STEM-EELS chemical composition mapping of the control film in fig. S9, weak signals of I, Br, and Pb are detected in the dark zones between the grains. In contrast, the sequential EELS chemical composition mapping of GBMP film (Fig. 3A) shows that the dark gaps with bubble-like structures are not only richer in C and N elements compared to the control film but also present less I, Br, and Pb contents. Therefore, we conclude that TTABr, mainly consisting of C and N, is located at GB sites in the upper part away from the bottom surface of the GBMP film, in keeping with the finding that the dark gaps are wider than those in the control film. We posit that TTABr possibly inserts its bromine substituents into the halide vacancies of metal halide perovskites at GBs. This interaction may be explained by a Lewis acid–Lewis base type interaction between undercoordinated Pb and lone pair–containing nitrogen as established by systematic shifts in the core-level binding energies corresponding to Pb, N, and Br atoms revealed by x-ray photoelectron spectroscopy (fig. S10) (*39*–*41*). The N → Pb interaction is further supported by vibrational spectroscopy (fig. S11).

To explore whether the intervention of TTABr influences the grain orientations, we applied depth-dependent grazing incidence XRD (GIXD) on the control and GBMP films through varying the x-ray incidence angle. The 2D pattern in fig. S12A and the integral GIXD profile in fig. S12B show that TTABr is of amorphous nature, in good agreement with the TEM results. The arc shape in 2D GIXD patterns both at a shallow incidence angle of 0.2° (fig. S12, C and G) and a larger incidence angle of 0.6° (shown in Fig. 3, B and C) indicates the random orientation of the grains from the surface and within the bulk, manifesting the inherent polycrystallinity of the perovskite films (*42*). For the GIXD integral line files in Fig. 3 (D and E) at various grazing incident angles from 0.2° to 0.6°, neither an obvious peak shift nor a new diffraction peak is obtained in the GBMP film in comparison with the control. We therefore conclude that the large TTABr molecule could not incorporate into the 3D perovskite structure, which is also consistent with the presence of TTABr at GBs observed in STEM-EELS measurements.

The influence of TTABr intervention on the crystallization process

To explore the time course of the crystallization process, we performed in situ GIXD while annealing the control and GBMP samples. A series of 2D GIXD images acquired at different stages of annealing (100°C) are shown in fig. S13, as well as in movies S1 and S2. In both cases, the scattering features at $q \sim 0.46$ Å^{-1}, $q \sim 0.50$ Å^{-1}, and $q \sim 0.64$ Å^{-1} that can be indexed to FA(MA)X-PbX_2-DMSO(DMF) intermediate adducts (X = Br^- and I^-) and the diffraction feature at $q \sim 1.0$ Å^{-1} corresponding to the 3D perovskite phase are observed (*42*, *43*). 2D GIXD profiles acquired from the control sample reveal the presence of discrete Bragg spots, which are suppressed by the presence of TTABr in the GBMP sample (fig. S13, A and D). From this observation, we surmise that TTABr molecules interact with the intermediate adduct and interrupt the alignment of corner-sharing $[PbI_6]^{4-}$ octahedra in certain directions over an extended range. The scattering features from the intermediate phases diminish with time, whereas the features corresponding to the 3D perovskite phase intensify, indicating the transformation of the adducts into the 3D perovskite phase.

We further analyzed the transformation of adducts into the perovskite phase from the time-resolved integral GIXD profiles shown in fig. S14 by estimating the integrated intensity of diffraction peaks through Gaussian fitting. The peak intensity profiles reveal relatively slower kinetics for the transformation of adduct into the 3D perovskite phase due to the presence of the TTABr, resulting in larger perovskite grains, thus lowering the GB density for GBMP films. This is further supported by color evolution of the control and GBMP films upon annealing, shown in fig. S15A. We propose a scheme demonstrating how TTABr influences the crystallization and growth of various phases during the formation process (Fig. 3, F and G, and fig. S15B).

GB mitigation–induced variety in optoelectronic properties of perovskites

To understand the influence of the GB mitigation on the optoelectronic properties of perovskite films, we quantified the hole mobility, trap densities by space charge–limited current (SCLC) measurement in fig. S16 (A to C), charge carrier lifetimes by time-resolved photoluminescence (TRPL), and energetic disorder using photothermal deflection spectroscopy (PDS). We obtained hole mobilities of 10.51 and 6.24 $cm^2\ V^{-1}\ s^{-1}$ for the GBMP and control device, respectively, confirming the enhancement of the hole mobility caused by the unique GB mitigator TTABr. In addition, the trap density in the GBMP film is calculated to be 2.25×10^{15} cm^{-3}, less than half of that for the control (6.87×10^{15} cm^{-3}). The charge carrier lifetime increased over 10-fold from 340 ns for the control to 4.2 μs for the GBMP film (fig. S16D), demonstrating the marked suppression of nonradiative carrier recombination by TTABr. By measuring the sub-bandgap absorption using PDS, we estimated the energetic disorder of perovskite films (fig. S16, E and F). The lower Urbach energy (E_U = 14.2 meV) for GBMP films as compared to the control films (E_U = 15.1 meV) proves less energetic disorder of the GBMP films.

The GBMP film in a complete solar cell architecture, i.e., with electron transport layer and hole transport layer, showed more than a doubled higher-average PL quantum yield (PLQY) (fig. S16G), demonstrating that its superior optical quality is maintained even when the perovskite film is embedded between electron and hole transport layers. From the PLQY, the quasi-Fermi level splitting $\Delta E_F\ q^{-1}$ can be determined, which is the internal V_{OC} of the absorber layer and represents the maximum V_{OC} that a device can achieve. From the PLQY increase, an average $\Delta E_F\ q^{-1}$ increase of ~24 mV is determined (fig. S16, H and I), which matches the trend of the device V_{OC} values as discussed further below. In summary, improved charge carrier dynamics, minimization of defects, low energetic disorder, and increased luminescence quantum yield suggest that the GB mitigation has desired effects on the optoelectronic properties of the perovskite films.

Device architecture and photovoltaic performances

We fabricated the regular mesostructured PSCs to evaluate the relationship between GB mitigation and device performance. In a fully

Downloaded from https://www.science.org at Universitat Autonoma de Barcelona on February 01, 2023

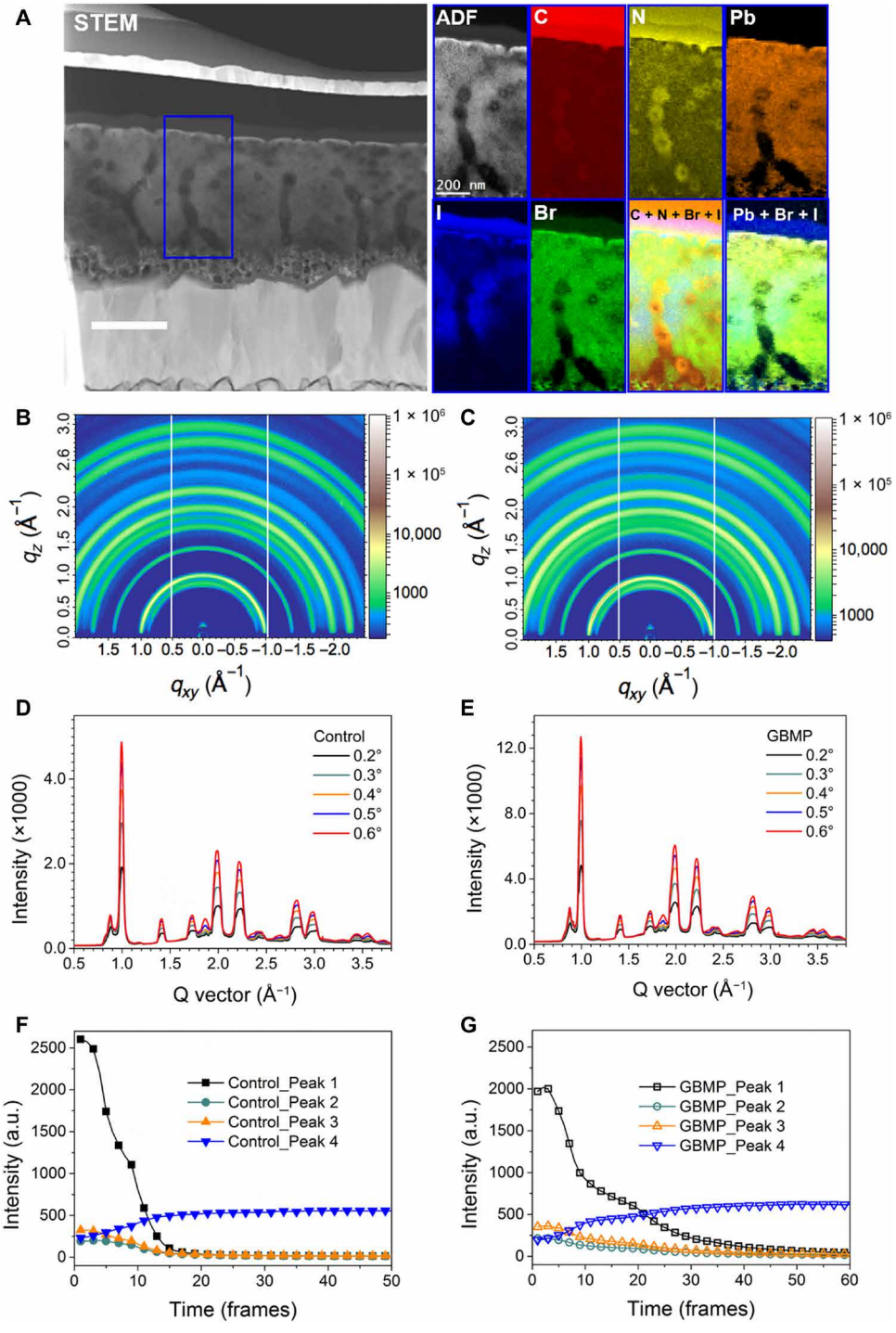

Fig. 3. The STEM-EELS chemical composition mapping and GIXD for perovskite films. (**A**) Left: Low-magnification ADF image showing the cross-sectional structure of a GBMP-based lamella. Scale bar, 500 nm. Right: EELS chemical composition mapping obtained from the blue rectangle area on the left ADF micrograph including individual elemental mapping for C (red), N (yellow), Pb (orange), I (blue), and Br (green) and composite distribution mapping. (**B** and **C**) 2D GIXD images with the x-ray incidence angle of 0.6° for the control (B) and GBMP (C) films. (**D** and **E**) Integral GIXD profiles at various incidence angles for films corresponding to (D) and (E), respectively. (**F** and **G**) The intensity of the characteristic peaks of films without (F) and with (G) TTABr annealed at 100°C as a function of time (frames), where peaks 1 to 3 are indexed to intermediate adducts, and peak 4 is referred to the typical perovskite phase. a.u., arbitrary units.

Downloaded from https://www.science.org at Universitat Autonoma de Barcelona on February 01, 2023

assembled device shown in Fig. 4A, TTABr an organic hole conductor could facilitate the hole transfer process owing to its favorable energy levels as confirmed by ultraviolet photoelectron spectroscopy (UPS), cyclic voltammetry (CV), and steady-state PL spectra, as shown in Fig. 4B and fig. S16 (J to L). Figure 4C shows the statistics of photovoltaic metrics for the control and GBMP-based PSCs. The GB mitigation in the GBMP film results in substantial improvements of the photovoltaic performance. Comparing to the control devices, key metrics, including V_{OC} and FF, have been improved simultaneously without compromising on the short-circuit current density (J_{SC}). On the basis of the optimized TTABr concentration (table S1) along with careful device engineering, we achieved the

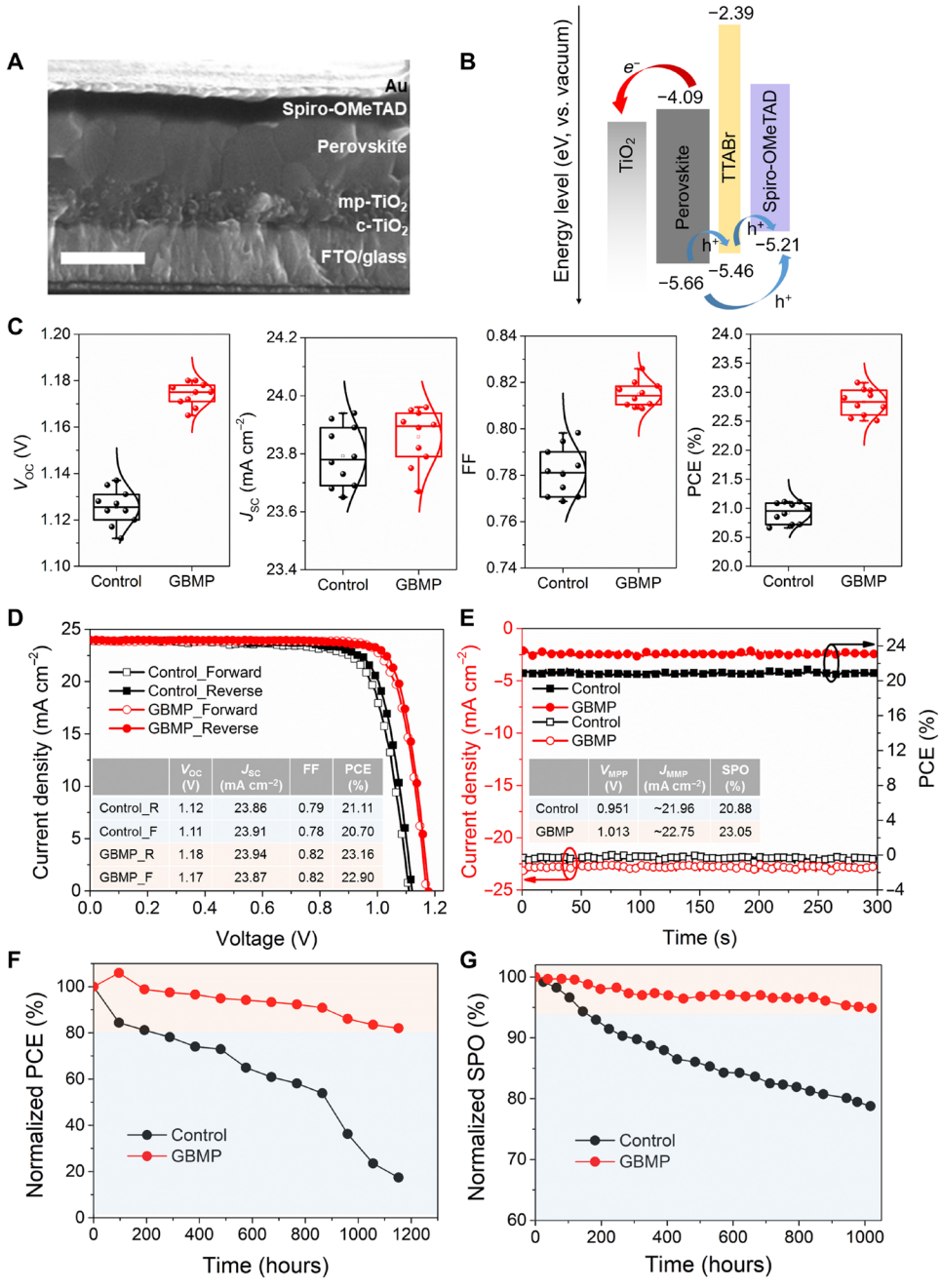

Fig. 4. Enhanced photovoltaic performances. (**A**) Cross-sectional SEM image of a typical GBMP-based device. Scale bar, 500 nm. (**B**) Energy level alignment diagram of TiO_2, perovskite, TTABr, and spiro-OMeTAD. (**C**) V_{OC}, J_{SC}, FF, and PCE metrics and statistics of the devices fabricated with the control and GBMP films from the same batch. (**D**) *J-V* curves for the champion control device and GBMP-based device measured in forward and reverse scans under simulated AM 1.5G illumination of 100 mW cm^{-2}. (**E**) The stabilized photocurrents and SPOs of the two abovementioned devices at the MPP. (**F**) Thermal stability results of the nonencapsulated typical control and GBMP-based devices after aging for more than 1100 hours at 85°C in a nitrogen atmosphere. (**G**) MPP tracking of the nonencapsulated control and GBMP-based devices at room temperature under continuous 1-sun-equivalent white light-emitting diode arrays (with no ultraviolet filters) in a nitrogen atmosphere.

Downloaded from https://www.science.org at Universitat Autonoma de Barcelona on February 01, 2023

champion device with a GBMP film, delivering an efficiency of 23.16% (reverse scan) with negligible hysteresis (a PCE of 22.90% in the forward scan) and a stabilized power output (SPO) of 23.05% at the maximum power point (MPP) under 1-sun AM 1.5G irradiance (Fig. 4, D and E). By contrast, the control device shows a lower SPO of 20.88%. The incident photon-to-electron conversion efficiency (IPCE) spectra, as shown in fig. S17, yield an integrated J_{SC} of ~23.4 mA cm^{-2} in accordance with the *J*–*V* data, showing the absence of any serious spectral mismatch between simulated and the actual sunlight.

Further analysis (figs. S18 to S22) establishes that the highly beneficial effect of TTABr on the photovoltaic metrics, in particular, the V_{OC} and FF, extends over a wide range of perovskite compositions and device architectures, demonstrating the versatility of our strategy. The fact that the PCE improvement arises predominantly from an increase in the V_{OC} and FF is in keeping with the reduction of defect concentration, prolonged charge carrier lifetime, and enhanced intergrain hole transfer as a result of GB mitigation in GBMP films. The trends observed for the V_{OC} values and the Fermi level splitting determined from the absolute PL efficiency are in agreement (fig. S16I), implying that the V_{OC} increase arises mainly from the reduction in trap-assisted nonradiative radiation. The small difference for the control film is caused by energy level misalignment (*44*), which is reduced for the GBMP film (Fig. 4B).

We probed the thermal stability of nonencapsulated control and GBMP-based devices at 85°C in a nitrogen atmosphere and present the results in Fig. 4F. This test follows the International Summit on Organic Photovoltaic Stability-Dark storage-Intrinsic stability at elevated temperature (ISOS-D-2I) protocol proposed in a recent consensus statement to address the intrinsic stability of PSCs in inert atmosphere (*45*). GBMP-based devices show superior thermal stability as the devices retained more than 80% of their initial PCEs after annealing at 85°C for >1150 hours, while the control devices degraded severely over the same time period, retaining <20% of their initial PCEs. We also tracked the MPP of the nonencapsulated control and GBMP-based devices under continuous full-sun-intensity illumination, and results are presented in Fig. 4G. This test follows the ISOS-L-1I (with electrical bias) protocol. The spectrum of the light-emitting diode array is shown in fig. S23A. GBMP-based devices show excellent operational stability, maintaining more than 90% of their initial SPO after 1000 hours, whereas the control shows a faster degradation, with their PCE decreasing to less than 80% of their initial values over the same time period. From the larger water droplet contact angle of 38.2° measured for the GBMP sample as compared to 12.1° for the control film, we anticipate better water resistance of GBMP-based PSCs due to the hydrophobicity of TTABr. We confirm experimentally that under exposure of devices to a relative humidity of ~50 ± 10% at ~24° ± 4°C, the GBMP-based PSCs retained ~90% of their initial PCE values after 15 days, whereas the control device lost more than 50% of its initial efficiency within 6 days, as shown in fig. S23B [ISOS-Dark storage-Stability in the ambient condition (ISOS-D-1)]. Thus, by combining a series of tests, we provide clues rendering a clear picture of the device performance enhancement through GB mitigation.

DISCUSSION

In summary, our study opens up new perspectives on mitigating GBs in polycrystalline perovskite films ranging from the nanoscale genuine (intra-aggregate) GBs to submicron-scale interaggregate GBs. The mitigation of GBs by modulating the crystallization kinetics using the judiciously designed mitigator TTABr led to the formation of perovskite films exhibiting low trap-state density and energetic disorder, reduced nonradiative recombination, and improved PLQY, which are beneficial for realizing highly efficient and stable PSCs. TTABr also accelerates intergrain hole transfer and charge carrier collection and thus amplifies the V_{OC}, FF, and PCE of the PSCs, which can be extended to various perovskite compositions and device architectures. The in-depth structural characterization not only clarifies the existing terminology in the perovskite field but also puts forth a new perspective to modulate GBs. Our results indicate that full-scale GB mitigation is particularly notable and promising to boost the quality of optoelectronic devices and are likely to find applications in the engineering of a whole range of polycrystalline materials.

MATERIALS AND METHODS

Materials

Methylammonium bromide (MABr), formamidinium iodide (FAI), methylammonium chloride (MACl), and titanium oxide paste (TiO_2 paste; 30 NR-D) were purchased from GreatCell Solar via Advanced Election Technology Co. Ltd. (China). Lead diiodide (PbI_2; 99.99%) and lead dibromide ($PbBr_2$; 99%) were purchased from Tokyo Chemical Industry Co. Ltd. 2,2′,7,7′-tetrakis(*N*,*N*-di-*p*-methoxyphenyl-amine)-9,9′-spirobifluorene (spiro-OMeTAD) was purchased from Merck. TTABr {^{1}H NMR (400 MHz, $CDCl_3$) δ: 7.47 parts per million (ppm) (dd, *J* = 8.6 Hz, 4.6 Hz, 8H), 7.38 to 7.32 ppm (m, 6H), 7.30 to 7.26 ppm (m, 4H), 7.15 ppm (d, *J* = 8.4 Hz, 4H), 7.11 ppm (d, *J* = 8.4 Hz, 8H), 7.08 to 7.02 ppm (m, 4H), and 6.99 ppm (d, *J* = 8.8 Hz, 4H); ^{13}C NMR (101 MHz, $CDCl_3$) δ: 147.39, 147.03, 146.58, 135.25, 132.45, 132.38, 129.59, 127.70, 127.66, 125.66, 125.49, 124.74, 124.63, 124.46, 123.59, 115.38, 115.18, and 77.36 ppm; high-resolution MS (atmospheric pressure chemical ionization/quadrupole orthogonal acceleration–time-of-flight) mass/charge ratio: $[M + H]^+$ calcd for $C_{54}H_{39}Br_3N_3^+$ 969.0575; found 969.064} was obtained from Chilworth Technical Centre, Merck Chemicals Ltd. (Southampton England). It is soluble not only in the antisolvent [chlorobenzene (CB)] during solution processing but also in the solvent of perovskite precursor [the mixture of *N*,*N*-dimethylformamide (DMF) and dimethyl sulfoxide (DMSO)]. Bis(trifluoromethylsulfonyl)imide lithium salt (LiTFSI) and 4-*tert*-butylpyridine (tBP; 96%), titanium diisopropoxide bis(acetylacetonate) (75% in 2-propanol), cesium iodide (CsI; 99.95%), and bis(acetylacetonate) were purchased from Sigma-Aldrich. Poly(triaryl)amine (PTAA; molecular weight ≤ 6000 g mol^{-1}) was purchased from Xi'an Polymer Light Technology Corp (China). Some solvents including DMF (99.8%), DMSO (99.7%), 1-methyl-2-pyrrolidinone (NMP; 99%), CB (99.8%), dichloromethane, and acetonitrile (ACN; 99.8%) were purchased from Acros Organics. SnO_2 colloidal solution (15% in H_2O colloidal dispersion) was purchased from Alfa Aesar. All the reagents were used as received.

Preparation of compact and mesoporous TiO_2 layers and SnO_2 layer

Fluorine-doped tin oxide (FTO) glass substrates (NSG 10, Nippon Sheet Glass, Japan) were cleaned by ultrasonication in a special cleaning liquid (Hellmanex II, 2 volume percent in deionized water), acetone, and ethanol for 15 min, respectively, and then dried with dry

Downloaded from https://www.science.org at Universitat Autonoma de Barcelona on February 01, 2023

air flow. A compact TiO_2 (c-TiO_2) layer of ~30 nm was subsequently deposited on the clean FTO glass substrates via spray pyrolysis at 450°C from a precursor solution of 0.6 ml of titanium diisopropoxide bis(acetylacetonate) and 0.4 ml of bis(acetylacetonate) diluted in 9 ml of anhydrous ethanol and oxygen as a carrier gas. Then, a mesoporous TiO_2 (m-TiO_2) layer was deposited onto the c-TiO_2 layer by spin-coating a diluted TiO_2 paste [30 NR-D (w:w = 1:6 in ethanol)], which was later sintered at 450°C for 30 min in dry air flow. The substrates composed of FTO glass/c-TiO_2/m-TiO_2 were transferred into a glovebox containing dry air (25°C, humidity of <2%) after cooling to 150°C, aiming to complete perovskite film deposition.

For SnO_2-based PSCs, indium tin oxide (ITO) transparent conductive substrates were precleaned for the electron-extraction layer deposition. The SnO_2 layer was deposited with the process reported in our previous work (*46*).

Perovskite film fabrication

For the perovskite films with the composition of $FA_{0.851}MA_{0.149}PbI_{2.552}Br_{0.448}$(4.48 mol % excess PbI_2), the perovskite precursor solution was prepared by mixing FAI (1.14 M), PbI_2 (1.20 M), MABr (0.20 M), and $PbBr_2$ (0.20 M) in a mixed anhydrous solvent of DMF/DMSO (v:v = 4:1) or NMP/DMSO/DMF (v:v:v = 1:4:15). The precursor solution was spin-coated onto the FTO glass/c-TiO_2/m-TiO_2 or the ITO/SnO_2 substrates via a two-step program at 2000 rpm with a ramping rate of 200 rpm s^{-1} for 10 s and 6000 rpm with a ramping rate of 2000 rpm s^{-1} for 30 s, respectively. During the second step, 100 μl of CB that contains various concentrations of TTABr ranging from 0.5 to 2 mg ml^{-1} was dripped on the spinning substrate at 15 s before the end of this program. The film was then annealed at 100°C for 45 min.

For the perovskite films with the composition of $FA_{0.851}MA_{0.149}PbI_3$ with 4.48 mol % excess PbI_2, the perovskite precursor solution was prepared by mixing FAI (1.14 M), PbI_2 (1.40 M), MAI (0.20 M), and MACl (0.45 M) in a mixed anhydrous solvent of DMF/DMSO (v:v = 4:1). The film deposition process is the same as above. For the perovskite films with the composition of MACl-stabilized $FAPbI_3$, the perovskite precursor solution and films were prepared completely according to the process in our previous work (*47*), however, without any posttreatment.

Hole transporting layer and gold electrode deposition

To obtain the desirable solution of hole transporting material, spiro-OMeTAD was dissolved into CB (70 mM) and doped with LiTFSI (520 mg ml^{-1} in ACN) and tBP by a molar ratio of 0.5 and 3.3, respectively. Then, the solution was deposited on the perovskite film in a dry air glovebox with humidity of <2%, by spin-coating at 4000 rpm with a ramping rate of 2000 rpm s^{-1} for 20 s. Last, device fabrication was finished by thermally evaporating 80 nm of gold layer as an electrode contact, wherein the overlap area between the FTO and metal electrodes is 0.25 or 0.103 cm^2. The devices were stored in a dry air glovebox for the oxidation of spiro-OMeTAD before all the characterizations.

Solar cell characterization

The *J–V* curves and SPOs of the PSCs were recorded with a digital source meter (2400 Series SourceMeter, Keithley Instruments, USA). To reduce the mismatch between the simulated and actual solar spectrum to less than 2%, a 450-W xenon lamp (Oriel, USA) equipped with a Schott K113 Tempax sunlight filter (Praezisions Glas and Optik GmbH) was used as the simulated AM 1.5G standard light source for photovoltaic measurements. The exact light intensity was determined by a reference-calibrated Si diode equipped with an infrared cutoff filter (KG-3, Schott) before each measurement. During the measurement, a black-colored metal mask was used to define the photoactive area of 0.16 or 0.09 cm^2 to ensure the accuracy of the J_{SC} obtained from *J–V* curves. The IPCE measurements were carried out using a 300-W xenon light source (ILC Technology). The sweeping conditions are reverse scan (scan rate of 10 mV s^{-1} and no delay time) and forward scan (scan rate of 10 mV s^{-1} and no delay time). All the above measurements were performed in air at room temperature with nonencapsulated PSCs. The long-term SPO tracking of nonencapsulated PSCs in a nitrogen atmosphere at the MPP under 1-sun illumination at room temperature was measured by a homemade electronic board with an eight-channel MPP capability. The light source that consisted of an array of white light-emitting diodes was powered by a constant current, and no ultraviolet filters were used. The intensity of the light source was calibrated by a reference-calibrated Si diode equipped with a KG-3 filter, equivalent to 1-sun sunlight of 100 mW cm^{-2}. The setup was calibrated periodically using a Keithley 2602B source-measuring unit.

Mass spectroscopy

MS spectrum of TTABr was collected on a HITACHI-80 mass spectrometer.

NMR spectroscopy

^1H NMR and ^{13}C NMR spectra of TTABr were recorded on Bruker AvanceIII-400 MHz NMR spectrometer. Chemical shifts are reported in parts per million (δ). ^1H NMR spectrum was referenced to tetramethylsilane (0 ppm) or solvent residual peak (7.26 ppm for ^1H NMR) as an internal standard.

Photothermal deflection spectroscopy

For PDS measurements, a monochromatic pump light beam is shined on the sample [film on quartz substrate immersed in an inert liquid FC-72 Fluorinert (3M Company)], which, on absorption, produces a thermal gradient near the sample surface via nonradiative relaxation and induces heating. A fixed-wavelength continuous-wave laser probe beam is passed through this refractive index gradient, producing a deflection proportional to the absorbed light at that particular wavelength, which is detected by a photodiode and lock-in amplifier combination. Scanning through different wavelengths produces a complete absorption spectrum.

Photoluminescence quantum yield

PLQY was measured using an integrating sphere (Gigahertz-Optik), an Andor Kymera 193i spectrograph, and a 660-nm continuous-wave laser (OBIS, Coherent) set at 1-sun-equivalent photon flux (790-μm beam full width at half maximum, 330 μW); the PL signal was collected at normal incidence using an optical fiber. We used the technique described by de Mello *et al.* (*48*). For the calibration of the PLQY measurements, we used a halogen lamp (BN-LH250-V01, Gigahertz-Optik), and to proof the correctness of the calibration, we measured the PLQY of a dye solution of indocyanine green in DMSO in the same setup and measured PLQY values within 15% deviation from the literature values.

Downloaded from https://www.science.org at Universitat Autonoma de Barcelona on February 01, 2023

Steady-state PL and TRPL

The steady-state PL spectra were performed on an Edinburgh Instruments photoluminescence spectrometer (Edinburg, UK) additionally equipped with an integrating sphere. The TRPL spectra were measured via time-correlated single-photon counting using a LifeSpec II (Edinburgh Instruments) fluorescence spectrometer with a picosecond pulsed diode laser (EPL-510, Edinburgh Instruments) at 510-nm wavelength and 85-ps pulse width. The laser fluence used was 5 nJ cm^{-2}.

Cyclic voltammetry

CV curves were recorded on an electrochemical workstation (Autolab PGSTAT302N, Metrohm, Switzerland).

DSC and TG

The DSC and TG data of TTABr were obtained from a commercial equipment (Q600, TA Instruments, USA) with a heating rate of 5°C min^{-1} under nitrogen atmosphere.

Scanning electron microscopy

The surface and cross-sectional morphologies of the control and GBMP films coated on FTO glass/c-TiO_2/m-TiO_2 substrates were acquired using a high-resolution scanning electron microscope (Gemini-SEM 300). An electron beam accelerated to 5.0 kV was used with either the In-Lens or SE2 detector.

Transmission electron microscopy

All the lamellae for HRTEM, ADF, STEM, and EELS investigations were prepared from complete solar cell devices by focused ion beam (FIB) cutting. Before the sample preparation with the FIB cutting, a Pt/carbon layer was deposited on the Au electrode to protect the sample from milling damage. The lamellae were carefully thinned down with FIB by gradually decreasing the ion acceleration voltages, down to 1 keV for the latest step, then extracted from the complete devices, and lastly welded on the Cu grid. After that, the resulting samples were vacuum-sealed in separate sample boxes and stored in a N_2 glovebox before TEM inspection. We transferred the FIB-cut lamella into the TEM setup within 30 s after opening the sealed sample box. HRTEM, ADF, and STEM images were obtained using a FEI Tecnai F20 field-emission gun microscope with a 0.19-nm point-to-point resolution at 200.0 kV equipped with an embedded Quantum Gatan Image Filter for EELS analyses. To reduce the electron dose during the HRTEM characterization, we limited the total electron beam exposure time to within 5 s. All the HRTEM images were obtained in an exposure time of 0.5 s with a screen current of around 0.7 nA. We obtained dual-scan EELS spectra with an energy dispersion of 1 eV (the first scan ranging from 240 to 2290 eV and the second scan ranging from 550 to 2600 eV). These scans were used to cover the signals from all the elements presented in the layers (perovskite and TTABr). The used convergent angle and collection angle are 12.7 and 87.6 mrad, respectively. Specifically, we have used K-edge (284 eV) for C mapping, K-edge (401 eV) for N mapping, $M_{4,5}$-edges (619 eV) for I mapping, $L_{2,3}$-edges (1550 eV) for Br mapping, and $M_{4,5}$-edges (2484 eV) for Pb mapping during the EELS studies.

AFM and c-AFM

AFM and c-AFM measurements for the perovskite films deposited on FTO glass/c-TiO_2/m-TiO_2 substrates were conducted on the setup (Ntegra Prima, NT-MDT SI, Russia) under the contact mode in dark.

Wide-angle GIXD measurements

GIXD measurements for the perovskite films deposited on FTO glass/c-TiO_2/m-TiO_2 substrates and TTABr film deposited on Si substrate were conducted on beamline 7.3.3 at Advanced Light Source, Lawrence Berkeley National Laboratory. The wavelength of x-ray was 1.240 Å, and the scattering intensity was detected by a PILATUS 2M detector. For the in situ thermal heating GIXD experiment, the fresh samples removed from the spin coater were heated at 100°C. All the data were collected in a tiled mode with an exposure time of 1.0 s. For the control sample, there was no delay for frames 1 to 10, while the frame interval was set to 30 s for frames 11 to 50. For the GBMP samples, there was no delay for frames 1 to 20, and then the frame interval was changed to 30 s for frames 21 to 60. Data analysis was performed using IGOR Pro software with the Nika package.

Quantifying the effect of TTABr on defect density and hole mobility in the perovskite

Current density–versus–bias voltage curves of the hole-only devices with the architecture of ITO-coated glass/NiO_x/perovskite/PTAA/Ag were based on the control and GBMP films, where these two films were processed from the approach identifying with the device fabrication. Single-carrier hole-only devices were measured in the dark under bias from 0.0025 to 3.500 V and 3.500 to 0.0025 V using an electrochemical workstation (Autolab PGSTAT302N, Metrohm, Switzerland).

SUPPLEMENTARY MATERIALS

Supplementary material for this article is available at https://science.org/doi/10.1126/sciadv.abo3733

REFERENCES AND NOTES

1. J. Burschka, N. Pellet, S. J. Moon, R. Humphry-Baker, P. Gao, M. K. Nazeeruddin, M. Gratzel, Sequential deposition as a route to high-performance perovskite-sensitized solar cells. *Nature* **499**, 316–319 (2013).
2. Y. Tu, G. Xu, X. Yang, Y. Zhang, Z. Li, R. Su, D. Luo, W. Yang, Y. Miao, R. Cai, L. Jiang, X. Du, Y. Yang, Q. Liu, Y. Gao, S. Zhao, W. Huang, Q. Gong, R. Zhu, Mixed-cation perovskite solar cells in space. *Sci. China-Phys. Mech. Astron.* **62**, 974221 (2019).
3. Y. Cao, N. Wang, H. Tian, J. Guo, Y. Wei, H. Chen, Y. Miao, W. Zou, K. Pan, Y. He, H. Cao, Y. Ke, M. Xu, Y. Wang, M. Yang, K. Du, Z. Fu, D. Kong, D. Dai, Y. Jin, G. Li, H. Li, Q. Peng, J. Wang, W. Huang, Perovskite light-emitting diodes based on spontaneously formed submicrometre-scale structures. *Nature* **562**, 249–253 (2018).
4. K. Lin, J. Xing, L. N. Quan, F. P. G. de Arquer, X. Gong, J. Lu, L. Xie, W. Zhao, D. Zhang, C. Yan, W. Li, X. Liu, Y. Lu, J. Kirman, E. H. Sargent, Q. Xiong, Z. Wei, Perovskite light-emitting diodes with external quantum efficiency exceeding 20 per cent. *Nature* **562**, 245–248 (2018).
5. Y. Jia, R. A. Kerner, A. J. Grede, B. P. Rand, N. C. Giebink, Continuous-wave lasing in an organic–inorganic lead halide perovskite semiconductor. *Nat. Photon.* **11**, 784–788 (2017).
6. Y. Fang, Q. Dong, Y. Shao, Y. Yuan, J. Huang, Highly narrowband perovskite single-crystal photodetectors enabled by surface-charge recombination. *Nat. Photon.* **9**, 679–686 (2015).
7. W. Zhang, G. E. Eperon, H. J. Snaith, Metal halide perovskites for energy applications. *Nat. Energy* **1**, 16048 (2016).
8. Y. Rong, Y. Hu, A. Mei, H. Tan, M. I. Saidaminov, S. I. Seok, M. D. McGehee, E. H. Sargent, H. Han, Challenges for commercializing perovskite solar cells. *Science* **361**, eaat8235 (2018).
9. H. Tan, A. Jain, O. Voznyy, X. Lan, F. P. García de Arquer, J. Z. Fan, R. Quintero-Bermudez, M. Yuan, B. Zhang, Y. Zhao, F. Fan, P. Li, L. N. Quan, Y. Zhao, Z.-H. Lu, Z. Yang, S. Hoogland, E. H. Sargent, Efficient and stable solution-processed planar perovskite solar cells via contact passivation. *Science* **355**, 722–726 (2017).
10. W. D. Callister Jr., D. G. Rethwisch, *Materials Science and Engineering: An Introduction* (John Wiley & Sons Inc, ed. 8, 1985), vol. 3, p. 4.
11. H. J. Möller, H. P. Möller, J. H. Werner, *Polycrystalline Semiconductors: Grain Boundaries and Interfaces* (Springer Proceedings in Physics, 1989), vol. 1, pp. 2–3.
12. C. J. Arceneaux, Baton Rouge: Claitor, in *Proceedings 26th Annual Meeting Electron Microscopy Society of America* (Claitor's Publishing Division, 1968), vol. 44.

Downloaded from https://www.science.org at Universitat Autonoma de Barcelona on February 01, 2023

13. W. Nie, H. Tsai, R. Asadpour, J.-C. Blancon, A. J. Neukirch, G. Gupta, J. J. Crochet, M. Chhowalla, S. Tretiak, M. A. Alam, H.-L. Wang, A. D. Mohite, High-efficiency solution-processed perovskite solar cells with millimeter-scale grains. *Science* **347**, 522–525 (2015).
14. Z. Chu, M. Yang, P. Schulz, D. Wu, X. Ma, E. Seifert, L. Sun, X. Li, K. Zhu, K. Lai, Impact of grain boundaries on efficiency and stability of organic-inorganic trihalide perovskites. *Nat. Commun.* **8**, 2230 (2017).
15. J. Jeong, M. Kim, J. Seo, H. Lu, P. Ahlawat, A. Mishra, Y. Yang, M. A. Hope, F. T. Eickemeyer, M. Kim, Y. J. Yoon, I. W. Choi, B. P. Darwich, S. J. Choi, Y. Jo, J. H. Lee, B. Walker, S. M. Zakeeruddin, L. Emsley, U. Rothlisberger, A. Hagfeldt, D. S. Kim, M. Grätzel, J. Y. Kim, Pseudo-halide anion engineering for α-$FAPbI_3$ perovskite solar cells. *Nature* **592**, 381–385 (2021).
16. N. H. Nickel, N. M. Johnson, W. B. Jackson, Hydrogen passivation of grain boundary defects in polycrystalline silicon thin films. *Appl. Phys. Lett.* **62**, 3285–3287 (1993).
17. G. Harbeke, *Polycrystalline Semiconductors: Physical Properties and Applications* (Springer Series in Solid-State Sciences, 1984), vol. 5, pp. 77–94.
18. D. W. de Quilettes, S. M. Vorpahl, S. D. Stranks, H. Nagaoka, G. E. Eperon, M. E. Ziffer, H. J. Snaith, D. S. Ginger, Impact of microstructure on local carrier lifetime in perovskite solar cells. *Science* **348**, 683–686 (2015).
19. D. Luo, R. Su, W. Zhang, Q. Gong, R. Zhu, Minimizing non-radiative recombination losses in perovskite solar cells. *Nat. Rev. Mater.* **5**, 44–60 (2020).
20. Y. Shao, Y. Fang, T. Li, Q. Wang, Q. Dong, Y. Deng, Y. Yuan, H. Wei, M. Wang, A. Gruverman, J. Shield, J. Huang, Grain boundary dominated ion migration in polycrystalline organic–inorganic halide perovskite films. *Energy Environ. Sci.* **9**, 1752–1759 (2016).
21. Q. Sun, P. Fassl, D. Becker-Koch, A. Bausch, B. Rivkin, S. Bai, P. E. Hopkinson, H. J. Snaith, Y. Vaynzof, Role of microstructure in oxygen induced photodegradation of methylammonium lead triiodide perovskite films. *Adv. Energy Mater.* **7**, 1700977 (2017).
22. J. Huang, S. Tan, P. D. Lund, H. Zhou, Impact of H_2O on organic–inorganic hybrid perovskite solar cells. *Energy Environ. Sci.* **10**, 2284–2311 (2017).
23. K. Domanski, E. A. Alharbi, A. Hagfeldt, M. Grätzel, W. Tress, Systematic investigation of the impact of operation conditions on the degradation behaviour of perovskite solar cells. *Nat. Energy* **3**, 61–67 (2018).
24. G. W. P. Adhyaksa, S. Brittman, H. Āboliņš, A. Lof, X. Li, J. D. Keelor, Y. Luo, T. Duevski, R. M. A. Heeren, S. R. Ellis, D. P. Fenning, E. C. Garnett, Understanding detrimental and beneficial grain boundary effects in halide perovskites. *Adv. Mater.* **30**, 1804792 (2018).
25. M. Abdi-Jalebi, Z. Andaji-Garmaroudi, S. Cacovich, C. Stavrakas, B. Philippe, J. M. Richter, M. Alsari, E. P. Booker, E. M. Hutter, A. J. Pearson, S. Lilliu, T. J. Savenije, H. Rensmo, G. Divitini, C. Ducati, R. H. Friend, S. D. Stranks, Maximizing and stabilizing luminescence from halide perovskites with potassium passivation. *Nature* **555**, 497–501 (2018).
26. T. Liu, Y. Zhou, Z. Li, L. Zhang, M.-G. Ju, D. Luo, Y. Yang, M. Yang, D. H. Kim, W. Yang, N. P. Padture, M. C. Beard, X. C. Zeng, K. Zhu, Q. Gong, R. Zhu, Stable formamidinium-based perovskite solar cells via in situ grain encapsulation. *Adv. Energy Mater.* **8**, 1800232 (2018).
27. S. Jariwala, H. Sun, G. W. P. Adhyaksa, A. Lof, L. A. Muscarella, B. Ehrler, E. C. Garnett, D. S. Ginger, Local crystal misorientation influences non-radiative recombination in halide perovskites. *Joule* **3**, 3048–3060 (2019).
28. T. W. Jones, A. Osherov, M. Alsari, M. Sponseller, B. C. Duck, Y.-K. Jung, C. Settens, F. Niroui, R. Brenes, C. V. Stan, Y. Li, M. Abdi-Jalebi, N. Tamura, J. E. Macdonald, M. Burghammer, R. H. Friend, V. Bulović, A. Walsh, G. J. Wilson, S. Lilliu, S. D. Stranks, Lattice strain causes non-radiative losses in halide perovskites. *Energy Environ. Sci.* **12**, 596–606 (2019).
29. W. Li, M. U. Rothmann, Y. Zhu, W. Chen, C. Yang, Y. Yuan, Y. Y. Choo, X. Wen, Y.-B. Cheng, U. Bach, J. Etheridge, The critical role of composition-dependent intragrain planar defects in the performance of $MA_{1-x}FA_xPbI_3$ perovskite solar cells. *Nat. Energy* **6**, 624–632 (2021).
30. S. Cai, J. Dai, Z. Shao, M. U. Rothmann, Y. Jia, C. Gao, M. Hao, S. Pang, P. Wang, S. P. Lau, K. Zhu, J. J. Berry, L. M. Herz, X. C. Zeng, Y. Zhou, Atomically resolved electrically active intragrain interfaces in perovskite semiconductors. *J. Am. Chem. Soc.* **144**, 1910–1920 (2022).
31. M. U. Rothmann, J. S. Kim, J. Borchert, K. B. Lohmann, C. M. O'Leary, A. A. Sheader, L. Clark, H. J. Snaith, M. B. Johnston, P. D. Nellist, L. M. Herz, Atomic-scale microstructure of metal halide perovskite. *Science* **370**, eabb5940 (2020).
32. X. Zheng, Y. Hou, C. Bao, J. Yin, F. Yuan, Z. Huang, K. Song, J. Liu, J. Troughton, N. Gasparini, C. Zhou, Y. Lin, D.-J. Xue, B. Chen, A. K. Johnston, N. Wei, M. N. Hedhili, M. Wei, A. Y. Alsalloum, P. Maity, B. Turedi, C. Yang, D. Baran, T. D. Anthopoulos, Y. Han, Z.-H. Lu, O. F. Mohammed, F. Gao, E. H. Sargent, O. M. Bakr, Managing grains and interfaces via ligand anchoring enables 22.3%-efficiency inverted perovskite solar cells. *Nat. Energy* **5**, 131–140 (2020).
33. H. Min, M. Kim, S.-U. Lee, H. Kim, G. Kim, K. Choi, J. H. Lee, S. I. Seok, Efficient, stable solar cells by using inherent bandgap of α-phase formamidinium lead iodide. *Science* **366**, 749–753 (2019).
34. D. Luo, W. Yang, Z. Wang, A. Sadhanala, Q. Hu, R. Su, R. Shivanna, G. F. Trindade, J. F. Watts, Z. Xu, T. Liu, K. Chen, F. Ye, P. Wu, L. Zhao, J. Wu, Y. Tu, Y. Zhang, X. Yang, W. Zhang, R. H. Friend, Q. Gong, H. J. Snaith, R. Zhu, Enhanced photovoltage for inverted planar heterojunction perovskite solar cells. *Science* **360**, 1442–1446 (2018).
35. E. H. Jung, N. J. Jeon, E. Y. Park, C. S. Moon, T. J. Shin, T.-Y. Yang, J. H. Noh, J. Seo, Efficient, stable and scalable perovskite solar cells using poly(3-hexylthiophene). *Nature* **567**, 511–515 (2019).
36. D. Zhang, Y. Zhu, L. Liu, X. Ying, C.-E. Hsiung, R. Sougrat, K. Li, Y. Han, Atomic-resolution transmission electron microscopy of electron beam-sensitive crystalline materials. *Science* **359**, 675–679 (2018).
37. Q. Jeangros, M. Duchamp, J. Werner, M. Kruth, R. E. Dunin-Borkowski, B. Niesen, C. Ballif, A. Hessler-Wyser, In situ TEM analysis of organic-inorganic metal-halide perovskite solar cells under electrical bias. *Nano Lett.* **16**, 7013–7018 (2016).
38. T. W. Kim, S. Uchida, T. Matsushita, L. Cojocaru, R. Jono, K. Kimura, D. Matsubara, M. Shirai, K. Ito, H. Matsumoto, T. Kondo, H. Segawa, Self-organized superlattice and phase coexistence inside thin film organometal halide perovskite. *Adv. Mater.* **30**, 1705230 (2018).
39. N. K. Noel, A. Abate, S. D. Stranks, E. S. Parrott, V. M. Burlakov, A. Goriely, H. J. Snaith, Enhanced photoluminescence and solar cell performance via Lewis base passivation of organic–inorganic lead halide perovskites. *ACS Nano* **8**, 9815–9821 (2014).
40. R. J. E. Westbrook, T. J. Macdonald, W. Xu, L. Lanzetta, J. M. Marin-Beloqui, T. M. Clarke, S. A. Haque, Lewis base passivation mediates charge transfer at perovskite heterojunctions. *J. Am. Chem. Soc.* **143**, 12230–12243 (2021).
41. F. Zhang, D. Bi, N. Pellet, C. Xiao, Z. Li, J. J. Berry, S. M. Zakeeruddin, K. Zhu, M. Grätzel, Suppressing defects through the synergistic effect of a Lewis base and a Lewis acid for highly efficient and stable perovskite solar cells. *Energy Environ. Sci.* **11**, 3480–3490 (2018).
42. Q. Hu, L. Zhao, J. Wu, K. Gao, D. Luo, Y. Jiang, Z. Zhang, C. Zhu, E. Schaible, A. Hexemer, C. Wang, Y. Liu, W. Zhang, M. Gratzel, F. Liu, T. P. Russell, R. Zhu, Q. Gong, In situ dynamic observations of perovskite crystallisation and microstructure evolution intermediated from $[PbI_6]^{4-}$ cage nanoparticles. *Nat. Commun.* **8**, 15688 (2017).
43. K. Wang, M.-C. Tang, H. X. Dang, R. Munir, D. Barrit, M. De Bastiani, E. Aydin, D.-M. Smilgies, S. De Wolf, A. Amassian, Kinetic stabilization of the sol–gel state in perovskites enables facile processing of high-efficiency solar cells. *Adv. Mater.* **31**, 1808357 (2019).
44. P. Caprioglio, M. Stolterfoht, C. M. Wolff, T. Unold, B. Rech, S. Albrecht, D. Neher, On the relation between the open-circuit voltage and quasi-Fermi level splitting in efficient perovskite solar cells. *Adv. Energy Mater.* **9**, 1901631 (2019).
45. M. V. Khenkin, E. A. Katz, A. Abate, G. Bardizza, J. J. Berry, C. Brabec, F. Brunetti, V. Bulović, Q. Burlingame, A. Di Carlo, R. Cheacharoen, Y.-B. Cheng, A. Colsmann, S. Cros, K. Domanski, M. Dusza, C. J. Fell, S. R. Forrest, Y. Galagan, D. Di Girolamo, M. Grätzel, A. Hagfeldt, E. von Hauff, H. Hoppe, J. Kettle, H. Köbler, M. S. Leite, S. Liu, Y.-L. Loo, J. M. Luther, C.-Q. Ma, M. Madsen, M. Manceau, M. Matheron, M. McGehee, R. Meitzner, M. K. Nazeeruddin, A. F. Nogueira, Ç. Odabaşı, A. Osherov, N.-G. Park, M. O. Reese, F. De Rossi, M. Saliba, U. S. Schubert, H. J. Snaith, S. D. Stranks, W. Tress, P. A. Troshin, V. Turkovic, S. Veenstra, I. Visoly-Fisher, A. Walsh, T. Watson, H. Xie, R. Yıldırım, S. M. Zakeeruddin, K. Zhu, M. Lira-Cantu, Consensus statement for stability assessment and reporting for perovskite photovoltaics based on ISOS procedures. *Nat. Energy* **5**, 35–49 (2020).
46. X. Yang, Y. Fu, R. Su, Y. Zheng, Y. Zhang, W. Yang, M. Yu, P. Chen, Y. Wang, J. Wu, D. Luo, Y. Tu, L. Zhao, Q. Gong, R. Zhu, Superior carrier lifetimes exceeding 6 μs in polycrystalline halide perovskites. *Adv. Mater.* **32**, 2002585 (2020).
47. Y. Zhang, Y. Wang, L. Zhao, X. Yang, C.-H. Hou, J. Wu, R. Su, S. Jia, J.-J. Shyue, D. Luo, P. Chen, M. Yu, Q. Li, L. Li, Q. Gong, R. Zhu, Depth-dependent defect manipulation in perovskites for high-performance solar cells. *Energy Environ. Sci.* **14**, 6526–6535 (2021).
48. J. C. de Mello, H. F. Wittmann, R. H. Friend, An improved experimental determination of external photoluminescence quantum efficiency. *Adv. Mater.* **9**, 230–232 (1997).
49. P. Ganesan, K. Fu, P. Gao, I. Raabe, K. Schenk, R. Scopelliti, J. Luo, L. H. Wong, M. Grätzel, M. K. Nazeeruddin, A simple spiro-type hole transporting material for efficient perovskite solar cells. *Energy Environ. Sci.* **8**, 1986–1991 (2015).
50. D. Braga, N. Battaglini, A. Yassar, G. Horowitz, M. Campione, A. Sassella, A. Borghesi, Bulk electrical properties of rubrene single crystals: Measurements and analysis. *Phys. Rev. B* **77**, 115205 (2008).
51. Z. Chiguvare, V. Dyakonov, Trap-limited hole mobility in semiconducting poly(3-hexylthiophene). *Phys. Rev. B* **70**, 235207 (2004).
52. W. Zhang, S. Pathak, N. Sakai, T. Stergiopoulos, P. K. Nayak, N. K. Noel, A. A. Haghighirad, V. M. Burlakov, D. W. deQuilettes, A. Sadhanala, W. Li, L. Wang, D. S. Ginger, R. H. Friend, H. J. Snaith, Enhanced optoelectronic quality of perovskite thin films with

Downloaded from https://www.science.org at Universitat Autonoma de Barcelona on February 01, 2023

hypophosphorous acid for planar heterojunction solar cells. *Nat. Commun.* **6**, 10030 (2015).
53. M. Sendner, J. Trollmann, A. Pucci, Dielectric function and degradation process of poly(triarylamine) (PTAA). *Org. Electron.* **15**, 2959–2963 (2014).
54. X. Yang, Y. Ni, Y. Zhang, Y. Wang, W. Yang, D. Luo, Y. Tu, Q. Gong, H. Yu, R. Zhu, Multiple-defect management for efficient perovskite photovoltaics. *ACS Energy Lett.* **6**, 2404–2412 (2021).
55. M. A. Green, A. Ho-Baillie, H. J. Snaith, The emergence of perovskite solar cells. *Nat. Photon.* **8**, 506–514 (2014).
56. R. T. Ross, Some thermodynamics of photochemical systems. *J. Chem. Phys.* **46**, 4590–4593 (1967).

Acknowledgments: The FIB sample preparation for (S)TEM experiments was conducted in the Laboratorio de Microscopias Avanzadas at Instituto de Nanociencia de Aragon-Universidad de Zaragoza. We acknowledge the LMA-INA for offering access to instruments and expertise. We acknowledge Z. Wang from École Polytechnique Fédérale de Lausanne (EPFL) for measuring SEM for SCLC, A. Agarwalla from EPFL for long-term MPP tracking, W. Yang from Peking University for analyzing the SEM and PLQY, and L. Ge from NT-MDT SI Beijing office for measuring AFM and c-AFM. **Funding:** This work was financially supported by Beijing Natural Science Foundation (JQ21005), the National Key R&D Program of China (2021YFB3800100 and 2021YFB3800101), the National Natural Science Foundation of China (91733301 and 62104221), the China Postdoctoral Science Foundation (2020M670036), and the R&D Fruit Fund (20210001). M.G. and S.M.Z. thank the King Abdulaziz City for Science and Technology (KACST) for financial support. M.I.D. acknowledges funding from the Royal Society. N.A. and R.H.F. thank the EPSRC project SUNRISE (EP/P032591/1). Q.H. and T.P.R. were supported by the U.S. Office of Naval Research under contract N00014-17-1-2241. Q.H. thanks the support from USTC Research funds of the Double First-Class Initiative (YD2100002007). We thank the support for sample preparation at Molecular Foundry of Lawrence Berkeley National Laboratory (LBNL), which is supported by the Office of Science, Office of Basic Energy Sciences, of the U.S. Department of Energy under contract no. DE-AC02-05CH11231. We also acknowledge the GIXD measurements at beamline 7.3.3 of Advanced Light Source (LBNL), which is a DOE Office of Science User Facility under contract no. DE-AC02-05CH11231. P.T. and J.A. acknowledge the funding from Generalitat de Catalunya 2017 SGR 327 and the Spanish MINECO project ENE2017-85087-C3. ICN2 is supported by the Severo Ochoa program from Spanish MINECO (grant no. SEV-2017-0706) and is funded by the CERCA Programme/ Generalitat de Catalunya. **Author contributions:** R.Z., L.Z., M.G., and Q.H. conceived the idea. L.Z., D.L., and R.Z. designed all the experiments. L.Z. fabricated and characterized the solar cells and prepared the samples for characterizations. P.T. and L.Z. conducted the TEM, STEM, and EELS. P.T., J.A., and L.Z. analyzed the TEM, STEM, and EELS. Q.H. measured and analyzed the GIXD. Y.L. synthesized extra TTABr and measured MS and NMR. N.A., M.I.D., and R.H.F. recorded and analyzed the PDS data. L.Z. measured and analyzed SCLC. L.Z. and D.L. measured and analyzed DSC and UPS. Q.G. and W.H. contributed to the analysis of characterizations such as AFM, c-AFM, and PL. A.H. provided the platform for long-term MPP tracking and contributed to the measurement. F.T.E. carried out the TRPL and PLQY measurements and analysis. S.M.Z., A.H., T.P.R., J.A., W.H., and Q.G. gave suggestions and comments. R.Z., M.G., and Q.H. directed and supervised the project. L.Z., D.L., Y.L., and M.I.D. wrote the manuscript. L.Z., D.L., P.T., J.A., W.H., Q.G., T.P.R., A.H., F.T.E., M.I.D., Y.L., Q.H., M.G., and R.Z. revised the paper. All the authors discussed the results and commented on the paper. **Competing interests:** The authors declare that they have no competing interests. **Data and materials availability:** All data needed to evaluate the conclusions in the paper are present in the paper and/or the Supplementary Materials.

Submitted 8 February 2022
Accepted 18 July 2022
Published 2 September 2022
10.1126/sciadv.abo3733

Downloaded from https://www.science.org at Universitat Autnoma de Barcelona on February 01, 2023

ScienceAdvances

Enabling full-scale grain boundary mitigation in polycrystalline perovskite solids

Lichen Zhao, Pengyi Tang, Deying Luo, M. Ibrahim Dar, Felix T. Eickemeyer, Neha Arora, Qin Hu, Jingshan Luo, Yuhang Liu, Shaik Mohammed Zakeeruddin, Anders Hagfeldt, Jordi Arbiol, Wei Huang, Qihuang Gong, Thomas P. Russell, Richard H. Friend, Michael Grtzel, and Rui Zhu

Sci. Adv., **8** (35), eabo3733.
DOI: 10.1126/sciadv.abo3733

View the article online
https://www.science.org/doi/10.1126/sciadv.abo3733
Permissions
https://www.science.org/help/reprints-and-permissions

Downloaded from https://www.science.org at Universitat Autnoma de Barcelona on February 01, 2023

Use of this article is subject to the Terms of service

Science Advances (ISSN) is published by the American Association for the Advancement of Science. 1200 New York Avenue NW, Washington, DC 20005. The title *Science Advances* is a registered trademark of AAAS.
Copyright © 2022 The Authors, some rights reserved; exclusive licensee American Association for the Advancement of Science. No claim to original U.S. Government Works. Distributed under a Creative Commons Attribution NonCommercial License 4.0 (CC BY-NC).